JOINT EUROPEAN TORUS

JET–P(90)04

G.A. Cottrell

Maximum Entropy and Plasma Physics

Maximum Entropy and Plasma Physics

G.A. Cottrell

JET-Joint Undertaking, Culham Science Centre, OX14 3DB, Abingdon, UK

** See Appendix 1*

Preprint of Paper to be submitted for publication in
Oxford University Press

MAXIMUM ENTROPY AND PLASMA PHYSICS

G.A.Cottrell

JET Joint Undertaking, Abingdon, Oxon., England. OX14 3EA

1. INTRODUCTION

Much of the driving force behind laboratory plasma physics research comes from the prospect of using controlled thermonuclear fusion, based on either inertial or magnetic confinement, to provide economically significant amounts of power. A magnetically confined high–temperature plasma is highly complex and, to make progress in our understanding of the fundamental plasma physics, one must be able to make accurate measurements of internal plasma parameters. Only then can theoretical ideas be confronted quantitatively with experiment. The specific goals of fusion impose stringent constraints on temperature, density and confinement and so give rise to extra problems for plasma diagnosis. For example, the high central temperatures of thermonuclear plasmas exclude direct measurements using intrusive material probes which are used mainly to monitor the cool exterior plasma regions. A wide range of non–intrusive physical measurement techniques has therefore been developed for diagnosis, ranging from basic measurements with electromagnetic probes, spectroscopy, particle and photon scattering, charge–exchange spectroscopy to nuclear particle and photon measurements. Most methods involve gathering data which has been transformed in some way either by the data collection geometry or by instrumental limitation and so inverse transformation is needed to obtain local plasma physics quantities.

In many measurements, the desirable high degree of line–of–sight access to the plasma has to be balanced against technological constraints; access is often restricted by the placement of magnetic field coils or other structures. In future reactor–like fusion devices, diagnostic access is likely to be further limited by the need to include first–wall and reactor blanket systems. Additional limitations arise in the measuring instruments themselves; typical examples are the finite spectral resolution of a visible

spectrometer and the truncation in the measured autocorrelation function in Fourier Transform spectroscopy. In these cases we are dealing with the problem of sparse data where the information is also corrupted by the inevitable noise. The use of linear inversion methods in this context can exaggerate defects in the data, in some cases leading to the appearance of unwanted transform–related artefacts in the reconstruction and in the worst cases give misleading results.

Here we consider the use of a radically different scheme for analysing difficult inverse problems. It is based on the idea that the unknown quantities that we wish to reconstruct from the data can be described in terms of positive, additive distributions. We note that a large number of plasma physics measurements belong to this category, for example, the number of particles per unit volume or the number of photons per unit wavelength. We ask: what is the most probable configurational arrangement of particles or photons in their respective cells of volume or wavelength interval that is consistent with the data that we have actually measured? The question is answered by maximizing the configurational entropy of the reconstruction subject to the constraint that the reconstruction be consistent with the measured data and its experimental uncertainties. Four different physical measurements, each involving an inverse transform in the analysis of diagnostic data from research in controlled thermonuclear fusion, are described and analysed within the framework of the maximum entropy (MAXENT) formalism. The generality of MAXENT is stressed; it is also applicable to many similar data analysis problems which are encountered outside the specfic field of plasma diagnosis. The four cases dealt with here are:

i) Inversion of Abel–transformed data,
ii) Deconvolution of electromagnetic line spectra,
iii) Fourier–transform spectroscopy and
iv) Two–dimensional tomographic reconstruction with sparse data.

To illustrate some of the the particular problems encountered in extracting information from laboratory plasmas, it is first necessary to give a brief overview of the essential features of experimental work in controlled magnetic fusion.

1.1 Overview of Controlled Thermonuclear Fusion

When nuclei of the isotopes of hydrogen, deuterium and tritium, come sufficiently close to one another, short range nuclear forces fuse them together resulting in the release of an alpha particle and a neutron. The nuclear rearrangement results in a reduction of total mass and release of binding energy which appears as kinetic energy of the reaction products:

$$D + T \rightarrow {}^{4}He\ (3.5\ MeV) + n\ (14.1\ MeV). \tag{1.1}$$

Before short–range nuclear forces can take effect, the mutual electrical repulsion of the nuclei must be overcome. This means that fusion reaction cross–sections are extremely small unless the relative velocities of the nuclei are high enough to overcome their electrostatic potential energy. For nuclei having a Maxwellian velocity distribution function, the high characteristic velocities needed to produce a high fusion reaction rate means that the temperature must be high and that the particles are in the fully ionized plasma state. To produce a significant reaction rate from (1.1), the plasma temperature, T, must be in excess of about 10 keV ($\equiv 10^8$ K). The possibility of using the DT reaction to form the basis of a fusion reactor is attractive since just 1kG of fuel would release 10^8 kWH of energy and would provide the requirements of a 1 GW (electrical) power station for a day.

The present goal of research in controlled thermonuclear fusion is to produce and study plasmas in conditions approaching those anticipated in an ignited deuterium–tritium reactor. To obtain a net energy gain in this system, the thermonuclear power must exceed the continuous loss of energy from the plasma. Energy losses occur through various mechanisms for heat conduction and particle convection across the confining magnetic field as well as through bremsstrahlung radiation. A measure of the quality of thermal insulation in a reactor can expressed in terms of the energy replacement time,

$$\tau_E = E / P, \tag{1.2}$$

where E is the total plasma energy and P the total power needed to sustain the plasma in a steady state. In a magnetic containment device, net energy gain from reaction (1.1) is given by the condition that the 'Lawson' product of the particle number density, n, and the energy replacement time be greater than $n\tau_E \approx 10^{20}$ m^{-3} s.

To achieve both this condition as well as that of high plasma temperature, the magnetic containment device known as a tokamak is widely considered to offer the most promise.

1.2 Overview of the Tokamak

In the tokamak configuration [1], plasma is confined in the geometry of a torus (or doughnut shape) and is perfectly symmetric about the major axis. Fig.1 shows its main features. Characterising the device is a strong toroidal magnetic field, B_T, generated by external coils supplemented by a second, weaker, poloidal field component, B_{p}, produced by a large current, I_{p}, flowing in the plasma itself. In the Joint European Torus (JET) tokamak [2], the toroidal field and plasma current can be as high as 3.5 Tesla and 7MA respectively. In addition, a third field in the vertical direction is needed to counteract the natural tendency of the plasma current ring to expand. The main toroidal field of the tokamak varies inversely with the major radius, R, of the torus as

$$B_T(R) = B_{T_0} R_0 / R, \tag{1.3}$$

where B_{T_0} is the magnetic field strength measured at the major radius of the plasma centre, R_0. The poloidal field, necessary for stability and equilibrium, combines vectorially with the toroidal field to produce a net helical field which winds around the torus. Without this helical twist, charge separation of particles gyrating about the field lines would set up a vertical electric field $\boldsymbol{E}$ which leads to a rapid outward drift of the plasma in the $\boldsymbol{E}\times\boldsymbol{B}$ direction. The combination of toroidal and poloidal magnetic fields gives rise to a set of nested, closed surfaces of constant magnetic flux on which the plasma ions and electrons move. In directions parallel to the flux surfaces the particle and thermal diffusivities are many times larger than those in the perpendicular direction; thus inhomogeneities in plasma pressure within a flux surface are rapidly smoothed out. This leads to a pressure gradient in the radial direction.

Apart from its role in providing a stable equilibrium, the plasma electron current also heats bulk plasma through collisional Joule dissipation. However, with increasing electron temperature, T_{e}, the plasma becomes increasingly collisionless and the electrical resistivity decreases (as $T_{\mathrm{e}}^{-3/2}$) so that, in some devices, Joule heating alone is not sufficient in producing the high temperatures required for fusion. Some form of additional plasma heating is therefore required of which there are two main

sources. One of these is the application of intense radio frequency wave energy to the plasma which is absorbed directly by resonant particles at their respective gyrofrequencies in the magnetic field. In JET, approximately 20MW of radio frequency heating power has been applied to the plasma in the ion cyclotron (25–50 MHz) frequency range. The other is that of neutral beam injection (NBI). With this, a beam of energetic neutral atoms (with energies $E_B >> kT$) is injected through the confining tokamak magnetic field into the plasma. Once there, the fast atoms are collisionally ionized, become trapped in the magnetic field and transfer their energy to the plasma by Coulomb collisions. In JET, 16 individual neutral hydrogen or deuterium beams have been used to deliver up to 20MW of power to the plasma. Both the radio frequency and NBI methods are proven and effective methods of supplimenting Joule heating and have been found experimentally to give similar plasma heating efficiencies.

2. ILLUSTRATION OF THE MAXIMUM ENTROPY METHOD

To introduce and illustrate the method of maximum entropy (MAXENT), a simple and commonly encountered problem has been chosen: inversion of Abel transformed data in tokamak measurements of the number density of electrons, n_e. The number density of electrons clearly belongs to the class of positive, additive distributions. The ideas discussed are, naturally, relevant to the determination of other positive, additive distributions. The signal detected by a diagnostic is composed of a local 'quantity of interest' which has been integrated along an instrumental line of sight through the plasma. In the present discussion, the 'quantity of interest' is the number density of plasma electrons. In a tokamak plasma, n_e is a function of the minor radius, r; the problem is to measure $n_e(r)$ given line–of–sight data for a number of different chords in the plasma. The information is used to infer the most likely radial distribution of n_e which gives rise to the measured data. Because electrons are assumed move essentially freely on flux surfaces, their distribution can be considered to be tied to the underlying structure of the magnetic flux surfaces and the problem becomes one of determining the radial distribution. With this geometry, the problem of inverting integrated line–of–sight data can then be attacked using the inverse Abel transform.

2.1 Measurement of electron density

One of the most successful and accurate of the class of non–intrusive plasma diagnostics involves the use of electromagnetic waves as a probe. Low intensity waves cause negligible perturbation to the plasma but still allow information about the internal plasma properties to be gathered with good spatial resolution. Here we are concerned with the refractive properties of the plasma, that is, the effect that the dielectric properties of the plasma have on electromagnetic wave propagation.

In a hot plasma the refractive index is governed by the population of free electrons and is given by

$$\mu^2 = 1 - \omega_p^2 / \omega^2 \tag{2.1}$$

where ω_p is the plasma frequency,

$$\omega_p = (n_e e^2 / \epsilon_0 m_e)^{1/2}, \tag{2.2}$$

e and m_e are respectively, the electron charge and mass, and ϵ_0 is the permittivity of free space. The refractive index of the plasma is typically measured using a Mach–Zhender interferometer [3], shown schematically in Fig.2. The device is a two–beam system with the plasma under study arranged to be in only one of the arms. A phase change,

$$\Delta\phi = \int (\mu - 1)\ (\omega\ /\ c)\ d\ell, \tag{2.3}$$

between the arms is related to the refractive index of the plasma, where c is the velocity of light and the integral is limited to that part of the plasma arm lying in the plasma. Measurement of the interferometer phase shift $\Delta\phi$ can thus be used to provide an estimate the mean refractive index of the plasma along the line of sight. Eq.(2.1) can be rewritten in the form,

$$\mu^{\,2} = 1 - n_e\ /\ n_c, \tag{2.4}$$

where the critical wave cut–off density is,

$$n_c = \omega^2\ m_e\ \epsilon_0\ /\ e^2. \tag{2.5}$$

By selecting a sufficiently high frequency ω for the probing wave, one can arrange that $n_e << n_c$ allowing Eq.(2.4) to be expanded to give $\mu \approx 1 - 1/2\ (\ n_e\ /\ n_c)$. The interferometer signal gives us a measure of the simple chord–averaged electron density,

$$\Delta\phi = (\omega\ /2cn_c) \int n_e\ d\ell. \tag{2.6}$$

Based on the principle outlined above, a practical (modified) version of the Mach–Zhender interferometric technique has been described earlier by Magyar [4].

2.2 The Discrete Abel Inversion

A recurrent problem in plasma diagnosis is to deduce local values of the quantity of interest from the available choral measurements. Naturally this problem is of much wider interest than just plasma diagnostics. We start by considering the geometry shown in Fig.3. Given a set of line integrated measurements of $\overline{n}_e(y)$ referring to a spatial distribution of electrons we wish to determine the unknown profile $n_e(r)$,

$$\bar{n}_e(y) = \int n_e(r)\, dx, \tag{2.7}$$

for a line–of–sight measurement made at height y above the midplane of the plasma.

The geometry shown in Fig.3 could represent, for example, a cross–section through a tokamak plasma. Initially let us assume the measured data to be ideal and noise–free. With lines of sight of the type shown, we construct a set of discrete radial shells where we assume the unknown number density of electrons n_{ej} to be constant in the j^{th} radial shell. The discrete form of Eq.(2.7) is,

$$\bar{n}_{ek} = \sum_{j=k}^{j_m} n_{ej}\, L_{jk}\,, \tag{2.8}$$

where L_{jk} is the incremental length of the k^{th} line–of–sight intersecting the j^{th} shell and j_m is the maximum shell index number corresponding to the total number of independent line–integral measurements, N. When j_m = N, the unknown set of discretized electron densities $\{ n_{ej} \}$ can be obtained from the matrix equation,

$$\{ \bar{n}_{ek} \} = \mathbf{L} \,.\, \{ n_{ej} \}, \tag{2.9}$$

by direct inversion,

$$\{ n_{ej} \} = \mathbf{L}^{-1} \,.\, \{ \bar{n}_{ek} \}, \tag{2.10}$$

where,

$$\mathbf{L} = \begin{bmatrix} L_{11} & . & . & . & . & . & . \\ L_{21} & L_{22} & & & & & \\ \vdots & \vdots & . & L_{jk} & & & \\ . & . & . & . & . & & \\ L_{j_m 1} & . & . & . & . & L_{j_m N} \end{bmatrix} . \tag{2.11}$$

With matrix inversion, solution of the linear Abel problem is robust when the measured data are noise–free and gives an effective radial resolution on the reconstructed density profile equivalent to the line–of–sight chord spacing. However, when only a sparse set of measurement chords is available, the quality of the reconstruction is limited, particularly when the data is corrupted by noise and errors.

The form of Eqs.(2.10) and (2.11) show how errors in the data will propagate from the outermost to the innermost region of the reconstruction. This effect causes the most interesting (central) regions of the profile to be the most severely in error. Linear inversion also gives no means of supressing negative–valued solutions which, in the present example of counting electrons, would clearly be unphysical. Indeed, as is shown in the example inversions of both trial and real tokamak data below, the linear method can produce negative–valued solutions with realistic data.

2.3 The Maximum Entropy Method

We now examine the non–linear maximum entropy (MAXENT) method of analysis and see how it can give an improved solution. The method presents a radically different approach in solving our Abel inversion problem. Instead of starting with the measured data and back–transforming it linearly using the inverted geometry matrix we start, instead, by considering the set of possible electron density profiles which, when transformed forward (using **L**), agree with the measured data. From this set (whose Abel transform agrees with the data and its errors), we select a representative member for display. In the MAXENT formulation, the representative member is the (positive–valued) electron density profile which has the maximum configurational entropy,

$$S = -\Sigma\, p_j \log\,(\, p_j \,/\, m_j\,), \tag{2.6}$$

where,

$$p_j = \frac{n_{\mathrm{e}j}}{\Sigma\, n_{\mathrm{e}j}}, \tag{2.7}$$

and m_j is an initial estimate or default level. The configurational entropy S is a measure of the missing information in a particular arrangement $\{\, n_{\mathrm{e}j} \,\}$ of electron density amongst the cells j. By maximising S subject to the constraint that the Abel transform of the electron distribution fits the measured data, the resulting reconstruction will contain the least amount of configurational structure (in the sense defined in Eq.(2.6)) and yet will remain consistent with the measured data and its associated errors. We note also that the logarithmic form appearing in Eq.(2.6) automatically ensures the reconstruction to be positive–valued. The displayed MAXENT reconstruction therefore will contain the least amount of spurious structure,

artefacts and noise and only such information as is necessary to fit the measured data is present. Consistency of the MAXENT solution with the data can be obtained by fitting using the χ^2 statistic,

$$\chi^2 = \sum_k (\mathbf{L}_{jk}\, n^{\mathrm{m}}_{\mathrm{e}j} - \bar{n}_{\mathrm{e}k}) \;/\; \sigma^2_k, \tag{2.8}$$

where $\{\, n^{\mathrm{m}}_{\mathrm{e}j} \,\}$ is a set of mock data used during iteration to find the solution and σ^2_k the variance (due to noise) on the k^{th} datum. Starting with a constant initial default level, an iterative MAXENT algorithm [5] was used to find the constrained maximum of S. Iteration was stopped when a value of $\chi^2/\mathrm{N} = 1$ was reached.

2.4 Results of Abel Inversion

To test MAXENT and compare results with linear inversion, both methods have been used to reconstruct four simulated and representative radial electron density distributions (Fig. 4). The advantage of using simulated data is that it becomes possible to judge the fidelity of the MAXENT reconstruction objectively by direct comparison with the original. A total of N=24 parallel lines of sight were used to generate line–integral data for each density profile. Then a constant level of normally–distributed random noise was added to each simulated line–integral value to simulate random errors on real experimental data. In the flat–profile example (Fig.5), both methods gave reasonable reconstructions, however, the MAXENT solution also showed noise suppression. Fig.6 shows the example of the hollow cylinder. This arrangement of emissivity could simulate line radiation in a tokamak from an impurity species in a certain charge state in one radial band. Here, again, MAXENT showed a superior noise performance, particularly in the zero signal region $0 < r < 12.0$, where the matrix solution displayed large amplitude positive and negative fluctuations. Similar features were also found for the case of the cylinder (Fig.7) and the plasma profile (Fig.8). By comparing both MAXENT and matrix solutions with the original electron density distributions of Fig.4, it is possible to derive an effective signal–to–noise ratio on the reconstructions (Table I).

TABLE I

Signal–to–noise ratios on the final Abel inversions for a peak signal–to–noise ratio of 20:1 on the simulated line integral data.

Case	Matrix Inversion	MAXENT
1. Flat Profile	5.5	9.6
2. Hollow Cylinder	4.4	9.2
3. Cylinder	8.5	14.0
4. Plasma Profile	15.0	17.0

In each case the signal–to–noise ratio on the reconstruction was less than the maximum on the data, illustrating the expected amplification of noise described above. However, the signal–to–noise ratio in the MAXENT reconstructions was larger, on average, by about 70% than that obtained with matrix inversion.

The method has also been applied to Abel inversion of real visible light intensity data measured in the DITE [6] tokamak during experiments to test a magnetic 'bundle divertor', a device designed to reduce the impurity content of the plasma by diverting part of the plasma flow to an external dump plate. Line–of–sight spectroscopic data were obtained using a monochromator (tuned to of CIII impurity line radiation) and the plasma was spatially scanned using a rotating mirror device. Comparisons of impurity radiation behaviour were made with the magnetic divertor switched either on or off. The results of Abel inversion of the data are shown in Figs. 9 and 10. In the limiter (divertor–off) configuration both the matrix and MAXENT inversions showed carbon light emission to peak near the plasma boundary (radius $r =$ 20 cm). The fluctuation in emission at $r = 12$ cm seen on the matrix inversion is not seen on the MAXENT solution and appears to be a result of noise amplification; there was no evidence for a fluctuation in the raw data at the corresponding radius and so it should (and does) not appear in the MAXENT solution. In the divertor–on case (Fig. 10), both methods show that the carbon emissivity still peaks ar a radius $r \approx 20$ cm, however the matrix solution becomes significantly negative for $r < 8$ cm. This is a result of error and noise propagation towards the centre of the reconstruction. The

positivity constraint of the MAXENT method is strikingly clear in this example. Using MAXENT, the beneficial effect of the divertor in reducing the level of carbon impurities in the plasma centre could now clearly be seen.

In the limit of a very small number of chordal measurements, the degree of coupling between the data and the reconstruction can be weak. Large regions of the profile may become decoupled from the data and the few lines of sight may become strongly weighted to the tangency radii (in the geometry of Fig.3). Simple application of the MAXENT method with a constant initial default level in this case can lead to the presence of unphysical distortions (at radii corresponding to the tangency radii of the measurements). The problem arising from data coupling may, however, be overcome by including "prior" information on the nature of the distribution of electron density through the default level m_j. Here one can use a plausible model for the prior distribution and encode previous knowledge about the behaviour of electron density distributions in tokamaks before any MAXENT iteration takes place. It is important to note that MAXENT will not constrain the reconstruction to be equal to the prior, except in the trivial case where there is a complete absence of data. After iteration, this method does result in the production of a physically plausible profile. A description of the use of a prior with extremely sparse experimental data is given in Cottrell [7] and a discussion on the use of priors in MAXENT analysis by Gull [8].

3. SPECTROSCOPIC DECONVOLUTION

3.1 Zeeman Splitting of Emission Lines in a Tokamak

Plasma spectroscopy offers another important tool in obtaining data on the state of a plasma. Observation and identification of emission lines from the various atomic constituents in the plasma can yield information both on impurity concentrations as well as ion temperatures (from Doppler broadening measurements). More information still comes from observations of the Zeeman splitting of spectral emission lines from atoms in the magnetic field of a tokamak. In a field of strength B, the energy levels of an atom suffer the energy splitting,

$$\Delta E = \Delta(Mg)\ \mu_{\mathrm{B}}\ B, \tag{3.1}$$

where M is the total quantum number, g the Lande factor and μ_{B} the Bohr magneton. For spectroscopic observations perpendicular to the magnetic field direction, only the linearly polarized π component (centered on the unshifted line frequency and corresponding to transitions with zero change in the magnetic quantum number, $\Delta m = 0$) is observed. Parallel to the magnetic field, however, the spectral line is split into two circularly polarized σ components which appear symmetrically either side of the unshifted line frequency and correspond to $\Delta m = \pm 1$ transitions. In general, the relative intensities of the π and σ components vary according to the viewing direction and the direction of the magnetic field. There are two main applications of this effect in tokamak plasma physics research. Firstly, if the location of the atomic species in the plasma is known (in practice this could be achieved by 'seeding' the plasma with tracer atoms) then the measured Zeeman splitting may be used to determine the local magnetic field strength using Eq.(3.1). Conversely, when B is known (typically B can be estimated to within a few percent in a tokamak), then we can use the measured Zeeman splitting to determine the location of the atomic species. This is possible because of the monotonic variation of the toroidal field with major radius (Eq.(1.3)).

3.2 Deconvolution of instrumental blurring with MAXENT

In the experimental example of Zeeman splitting measurements, an optical multichannel analyser was used to survey visible emission from the JET tokamak plasma [9]. A raw experimental spectrum (together with the measured instrument function) is shown in Fig.11, and reveals a CrI line multiplet and CII lines. There was

almost 100% Zeeman modulation of the CrI λ4274 $\mathring{A}$ line but the CrI λ4254 $\mathring{A}$ line (which should also have been split) was apparently featureless. With an expected tokamak field strength $B \approx 3$ Tesla, the Zeeman σ components should have been split by $\Delta\lambda \approx 0.75$ $\mathring{A}$, a value close to the instrumental resolution (≈ 1 $\mathring{A}$). It thus became apparent that the fine spectral structure was being smoothed by the instrument function of the spectrometer.Thus in order to resolve the fine structure, deconvolution was essential.

In a spectrometer, the incoming (original) spectrum, f_j, is convolved with the instrumental blurring function, b_j, resulting in the blurred spectrum, F_j,

$$F_j = f_j * b_j = \sum_i b_i f_{j-i} \tag{3.2}$$

Deconvolution (i.e. the removal of the effects of this smearing), involves an inverse problem of estimating f_j given both the blurred data F_j and the instrument function b_j. A standard solution to the problem of inverting Eq.(3.2) is based on noting that, under Fourier transformation, convolution can be expressed as the product of two Fourier transforms

$$\text{F.T.}\{ F_j \} = \text{F.T.}\{ f_j \} \times \text{F.T.}\{ b_j \} \tag{3.3}$$

which shows a possible method of solution. There are two well known problems with this method of solution. Firstly, owing to data truncation, artefacts (or 'sidelobes') are introduced. Secondly, the linearly–deconvolved spectrum can become negative. In the MAXENT solution (Fig.12), both of these problems were avoided. MAXENT was applied to this problem in a way similar to that described in section 2 (above) except that in the forward–transform of the 'mock' spectral data, the convolution operation (Eq.(3.2)) was used. A striking feature of Fig.12 is the discovery that the deconvolved CrI λ4254 $\mathring{A}$ line now showed Zeeman splitting. Moreover, the magnitude of the splitting of the three CrI lines was now consistent with a single magnetic field of strength $B = 3.0 \pm 0.1$ Tesla (corresponding to the field at radius $R = 2.12$ m), and almost exactly coincident with the tangential radius of the viewing chord used in the experiment. Hence, the magnetic field inferred was nearly parallel to the viewing direction which explained the almost complete absence of the central π component. This can be seen particularly clearly with the deconvolved CrI λ4274 $\mathring{A}$ line in Fig.12.

4. FOURIER TRANSFORM SPECTROSCOPY

4.1 Measurement of Electron Cyclotron Emission from a Tokamak plasma

Hot thermal electrons (typically having temperatures in the range $T_e \cong$ 1–20 keV) are confined in the tokamak magnetic field (typically of strength $B \cong$ 1–5 Tesla) and gyrate around the magnetic field lines with the electron cyclotron frequency,

$$\omega_{ce} = e\,B\,/\,m_e. \tag{4.1}$$

The gyrating electrons radiate electron cyclotron emission (ECE) at the fundamental frequency ω_{ce} as well as at its harmonics, $2\omega_{ce}$, $3\omega_{ce}$ etc. Because the magnetic field in a tokamak decreases monotonically (Eq.(1.3)) with the major radius, ω_{ce} also varies with radius. Thus an observation of the frequency of ECE can be used to determine the radial location of a particular group of radiating electrons. Furthermore, as the plasma is optically thick to radiation at the fundamental and first harmonic ($\omega = 2\omega_{ce}$) of the electron cyclotron frequency, the electrons radiate energy at a level close to that of a blackbody in this frequency range,

$$I(\omega) \equiv I_b(\omega) = \omega^2\, kT_e\, /8\pi^3 c^2. \tag{4.2}$$

Thus an absolute measurement the ECE spectrum $I(\omega)$ is equivalent to a measurement of the radial distribution of the electron temperature in the plasma, $T_e(R)$. The physics of electron cyclotron emission has been discussed in more detail by Costley [10].

Measurements of ECE in tokamaks are often based on the technique of Fourier–transform spectroscopy (e.g. [11]). For typical tokamak parameters, ECE is observed in the frequency range 60–600 GHz. Experimentally, a two–beam Michelson interferometer is used to measure the autocorrelation function with a typical time sampling rate $\Delta t \approx$ 10 ms and frequency resolution $\Delta f \approx$ 10 GHz and rapidly scanned interferometer offers considerable advantages in terms of simplicity of frequency calibration and wide spectral range. However, it is well known that the exact spectrum of the incident radiation source can only be determined when the (noise–free) autocorrelation function has been measured for all values of the path difference between the two interfering wave trains. In any practical system, not only do we have to contend with noise on the data but also have no knowledge of the autocorrelation function beyond a certain maximum path difference, Nδ, limited by the scanning range

of the interferometer.

4.2 The Autocorrelation Function

In general, we require an estimate of the spectrum $I(\omega)$ of a radiation source. This is related to the measured autocorrelation function $A(\tau)$ by the Fourier integral,

$$A(\tau) = A_0 + \int_0^\infty I(\omega) \cos(\omega\tau)\, d\omega, \tag{4.3}$$

where τ is the time delay between the two interfering wave trains and A_0 a constant background level on the whole interferogram. In practice, the detector output of an interferometer is sampled discretely giving an estimate of the source spectrum,

$$I(\omega) = (2/\pi) \sum_{n=0}^{N} [A(n\Delta\tau - \tau_0) - A_0] \cos(\omega n \Delta\tau), \tag{4.4}$$

where τ_0 is an (initially) unknown offset representing the zero path difference (ZPD) correction between the two arms if the interferometer. Fig. 13 shows some typical autocorrelation data obtained in experiments [12] on the DITE tokamak using a millimetre–wavelength Michelson interferometer. The autocorrelation function Eq.(4.3) is sampled with the discrete time delays τ_0, $\Delta\tau - \tau_0$, $2\Delta\tau - \tau_0$, ..., $N\Delta\tau - \tau_0$. The maximum spectral resolution is inversely related to the maximum time delay,

$$\Delta\omega = 1/(N\Delta\tau - \tau_0). \tag{4.5}$$

Fig.14 shows the spectrum obtained by direct Fourier transformation of the raw data of Fig.13. Because no weighting was applied prior to transformation, the frequency resolution obtained is the maximum possible defined in Eq.(4.5). However, the spectrum also exhibits unphysical negative regions which are associated with artefacts ('sidelobes') caused by the truncation of the autocorrelation data. To reduce the magnitude of the sidelobes, it is common to weight (or 'apodize') the autocorrelation data prior to transformation. However, because short–wavelength Fourier components are weighted down strongly in this process, apodization also degrades the spectral resolution (by typically up to a factor of two). So, in choosing an apodization function, one is forced to compromise between resolution and a tolerable level of spurious structure. A standard apodization function is the cosine–squared weighting; the result of applying this function to the data prior to transformation are

shown in Fig.15. Although negative sidelobe structure was reduced, resolution was also degraded such that structure on the low frequency side of the main peak has been lost and the other harmonic peaks broadened.

4.3 Autocalibration with MAXENT

To solve the Fourier Transform Spectroscopy problem using MAXENT, we have adpoted the same basic method as was used above in the Abel inversion problem. Here the 'mock' autocorrelation data were calculated using the fast Fourier–transform and these were subsequently interpolated on to a grid at the exact time delays at which the real data were measured. The misfit between 'mock' and real data was then calculated using the χ^2 statistic, and, starting from a flat spectrum (i.e. m_j = constant), iteration was started. Fig.16 shows the development of the solution at various stages of iteration. After 12 iterations, $\chi^2/\mathrm{N} = 3.0$, but even after 20 iterations could not be reduced below 2.7. However the value of χ^2/N, at that stage, was not fully minimised with respect to changes in τ_0 , i.e. variations in τ_0 produce variations in the mock data after MAXENT iteration. Based on the spectra obtained after 15 iterations, χ^2/N was then minimised with respect to τ_0, resulting in a better value $\tau_0 = 4.6$ grid points. One further optimization enabled us to obtain $\chi^2/\mathrm{N} = 1.0$ with an optimum ZPD of $\tau_0 = 4.68$ grid points after 16 iterations (Fig. 17). In principle this calibration procedure can be applied iteratively. Unless the initial estimate of τ_0 was far from optimum, one or two recalibrations was generally found to be sufficient.

The resulting optimized MAXENT spectrum is shown in Fig.18. The spectrum has good resolution, shows the (known) structure on the low frequency side of the main harmonic peak and is everywhere positive. In this case, the low frequency structure was believed to be caused by instrumental resonance for which compensation could be applied *a posteriori* by comparison of the plasma spectrum with that of a laboratory blackbody.

5. TWO–DIMENSIONAL TOMOGRAPHY

5.1 Neutral Beam Tomography

During development of the technology of the JET neutral beam injection (NBI) system, it was important to ensure that angular spreading (beam divergence) of the neutral beam as it propagates away from the beam source should be below a strict limit as the size of the beam entrance ports into the tokamak was limited by mechanical constraints. At the beam centre (a few metres away from the source) the power density is ≈ 10–30 kW cm^{-2}, a level which would melt metallic probes and therefore rule out direct measurements of the beam quality for long–pulse (5–10 second) operation. It therefore became important to develop a different, non–intrusive, method of determining the spatial distribution of the neutral beam in a cross–sectional slice.

The method chosen [13] was to diagnose the beam optically using observations of the line radiation emitted by fast hydrogen ions and atoms (with energies up to 80 keV per amu and velocities up to $v_b \approx 3 \times 10^6$ m s^{-1}) in two collisional reactions with background molecules in the flight path of the beam:

1) Charge–exchange excitation collisions

$$\underline{H}^+ + H_2 \rightarrow \underline{H}^{0*} \rightarrow H_\alpha \text{ photon} \qquad (5.1)$$

2) Excitation of ground–state neutrals

$$\underline{H}^0 + H_2 \rightarrow \underline{H}^{0*} \rightarrow H_\alpha \text{ photon} \qquad (5.2)$$

where the underlined symbol denotes a fast beam particle and the asterisk an excited neutral (of quantum number n=3 for Balmer–alpha emission). By viewing light from the beam atoms at an angle to their direction of motion (typically 10–40^0), emission from fast particles could be separated spectroscopically from background light by means of their finite Doppler shift ($\Delta\lambda \approx 20$ Å) away from the H_α rest wavelength ($\lambda_0 = 6563$ Å). The optical emissivity of the fast particles is,

$$f(x, y) = n_b (x, y)\, n_0\, \sigma^*\, v_b, \qquad (5.3)$$

where $n_b(x, y)$ and n_0 are, respectively, the number density of fast particles and background hydrogen molecules in the path of the beam and σ^* the Balmer–alpha excitation cross–section for reactions (5.1) and (5.2). As the beam–plasma is optically thin, a single spectroscopic measurement through the beam is equivalent to a line–integral of the emissivity. Therefore a measurement of $f(x, y)$ can be related to the unknown density of beam atoms, $n_b(x, y)$. Spatial scanning of the Balmer–alpha beam emission was performed using a number of optical scanners arranged around the periphery of the beam flight tube (Fig.19) with each scanner sampling the H_α light emission using narrow–band interference filters. The measurement geometry therefore corresponds to chord–average samples from a set of fan–beams viewing from different positions.

The unknown two–dimensional neutral beam emissivity function, $f(x, y)$, is seen in projection along the viewing lines shown in Fig.19 giving a signal response at the k^{th} optical detector $(1 < k < M)$

$$d_k = \iint g_k(\varphi)\, r^{-1}\, f(x, y)\, dx\, dy \tag{5.4}$$

where $g_k(\varphi)$ is the calibrated angular response function of the k^{th} detector and φ the angle of the incoming photons with respect to the instantaneous pointing direction of the scanner. The fundamental problem in tomography is inversion of Eq.(5.4) which allows estimation of $f(x, y)$ from the data d_k. Quantizing $f(x, y)$ into a discrete set of values $\{f_j\}$ $(1 < j < N)$, and calculating matrix element contributions O_{jk} from the j^{th} pixel to the k^{th} detector, we obtain,

$$f_j = O_{jk}^{-1}\, d_k + n_k\,, \tag{5.5}$$

where n_k is the noise on the k^{th} datum. In the high signal–to–noise ratio limit, $n_k = 0$ and Eq.(5.5) could, in principle, be inverted linearly.

It was shown by Radon [14] that $f(x, y)$ cannot be determined completely for a finite number of projections; in this case the reconstruction must be bandwidth–limited. The central slice theorem [15] can be used to determine the information available when only a finite number of projections is available. The theorem states that, for parallel projections, the Fourier transform of a projection at angle γ is equal to the Fourier transform of the object evaluated along the line at angle γ passing through the origin. Thus to reconstruct an object with diameter D showing

spatial structure on the finest scale Δx, we would need,

$$n = \pi\, D \,/\, \Delta x, \tag{5.6}$$

continuous projections [16]. For projection data sampled according to the Nyquist criterion, there must be two samples per cycle of the highest spatial frequency present. Thus, of order $2D \,/\, \Delta x$ samples per projection are needed.

An important feature of the design of the NBI tomography system was the ability to be able to resolve structure in the peripheral region of the beam with maximum resolution as it is in this region that the beam focussing quality is most critical. Thus it was essential to use the full angular resolution of the scanners, equivalent to a value $\Delta x = \Delta y \approx$ 2 centimetres at the position of the beam. Meeting the condition of Eq. (5.6) in the geometry shown in Fig. 19, we would therefore have needed $n \approx$ 100 scanners each operating with full angular resolution. However technical considerations limited us to just 12. Thus in the present application the line–integral data were sparse and so we have used MAXENT to fill in the unmeasured regions of Fourier space.

5.2 Solution and autocalibration with MAXENT

In the MAXENT inversion, the 'mock' data were generated using the forward transform given by Eq.(5.4) and the χ^2 statistic as described in section 2.2. Starting from a constant default level, the inversion was calculated on a $64 \times 64 = 4096$ point mesh shown in Fig.19. During tests it was found that variations in mirror reflectivity, interference filter characteristics and photomultiplier tube efficiencies between the individual scanner units introduced systematic differences in the relative sensitivities. This was corrected in the analysis using the autocalibration feature of MAXENT. First, a reconstruction was calculated from an initially calibrated data set. In general, it was found that the value of χ^2/N was, at this stage, not fully optimized with respect to variations of a small set of sensitivity calibration factors, one for each of the cameras. By adjusting these, it was found that it was then possible to reduce the value of χ^2/N thus improving the consistency of the camera data with a single reconstruction. The development of the MAXENT solution in the 4096–dimension tomographic problem is shown in Fig. 20 after 1, 3, 5 and 15 iterations. Beyond 15 iterations, no significant changes ocurred to the solution as χ^2/N had reached unity at the 15th iterate. Worthy of note is the excellent reconstruction obtained with only 7

scanners operational (at positions C_1 – C_4, C_6, C_8 and C_{12} on Fig.19) and a signal–to–noise ratio of $\approx$ 100 on the raw camera data. An earlier numerical study [17] based on simulations of the beam geometry has allowed us to evaluate the fidelity of the results. With only 7 cameras, one would expect some distortion of the contours in Fig. 21 at a level about 10% of the peak level on the reconstruction. At the 50% level we might also expect to see small distortions related to the presence of noise on the raw data. The double peaks seen on Figs. 20 (b) and (c) are, however, real and evidence for them could be seen on the raw data. These peaks are related to a technical feature of the neutral beam source, the double physical structure of the electrostatic beam–forming grids, and to the focussing properties of the electrostatic lenses. Overall, the results indicated that the beam divergence was about 0.5^0 (below the upper limit of the design) and that the spatial spreading of the beam was within the design limits governed by the solid angle of the entrance port into the tokamak chamber.

6. CONCLUSIONS

The method of Maximum Entropy has been discussed for four problems in the field of plasma diagnostics. It has been found to offer advantages in the solution of an inverse problem where there is inadequate sampling of data, the noise on the data cannot be neglected or limitations are imposed by a measuring instrument. Most plasma diagnostic work is beset by a combination of the three problems. Maximum Entropy analysis offers a clear framework for dealing with such cases and can help us avoid producing spurious images of positive, additive quantities such as distributions of particle density or numbers of photons per unit wavelength. The study has revealed four clear advantages in using the MAXENT method over linear inversion methods:

(1) There is an enhancement in attainable resolution and signal–to noise ratio,
(2) Inversions are positive and contain no spurious transform–related artefacts.
(3) The only configurational structure which appears on an inversion is that for which there is evidence in the original data.
(3) The determination of (initially) poorly–known instrumental calibration factors is facilitated through the technique of autocalibration.
(4) Prior information about the object under reconstruction can be encoded in a simple way through the default level.

Other possibilities also exist in other plasma diagnostic problems where the Maximum Entropy method could also be used to advantage. These include reconstruction of other radially varying quantities in the plasma such as neutron and soft X–ray emissivities using imaging cameras and the principles described in section 5. Another possibility is reconstruction of the magnetic equilibrium in a tokamak. The Grad–Shafranov equation [1] is used to determine an optimum choice for the unknown functions of plasma current density $j(r)$ and plasma pressure $p(r)$ by matching predicted and measured magnetic fluxes at the plasma boundary. Often cubic spline functions are used as trial functions in this analysis which limits the reconstructions to a narrow class for which there may be no evidence in the data. The use of MAXENT in this context would free the solutions of this limitation and, apart from the benefits of positivity and noise supression, would enable the use of prior information. As an example, the knowledge that both j and p are zero at the boundary could be encoded simply in terms of the default level.

REFERENCES

[1] Wesson, J., *Tokamaks.* Oxford Engineering Science Series, **20**. Publ. Oxford Science Publications, Clarendon Press, Oxford. (1987).

[2] *The JET Project and the Prospects for Controlled Thermonuclear Fusion.* Phil. Trans. R. Soc. Lond. **A 322**, (1987)

[3] Hutchinson, I.H., *Principles of Plasma Diagnostics.* Cambridge University Press (1987).

[4] Magyar, G., In: *Plasma Physics and Nuclear Fusion Research.* pp 535. Publ. Academic Press (1981).

[5] Skilling, J., *Maximum Entropy and Bayesian Methods in Applied Statistics* Publ. Cambridge University Press. pp 179 (1984).

[6] Paul, J.W.M., et al. *Applications of High Temperature Plasma Physics* Phil. Trans. R. Soc. Lond. **A 300**, 535, (1987).

[7] Cottrell, G.A., Fairbanks, E.S. and Stockdale, R.E. *Rev. Sci. Instrum.*, **56(5)**, Part II, 984. (1985).

[8] Gull, S.F., *Maximum Entropy and Bayesian Methods.* Ed.J. Skilling, Publ. Kluwer Academic Publ., 53. (1989).

[9] Carolan, P.G., Forrest, M.J., Peacock, N.J. and Trotman, D.L., *Plasma Physics and Controlled Fusion*, **27(10)**, 1101. (1985).

[10] Costley, A., In: *Diagnostics for Fusion Reactor Conditions.* Vol I, 129. EUR 8351–I EN (1982).

[11] Lipson, S.G., and Lipson, H., *Physical Optics*, Publ. Cambridge University Press (1981).

[12] Cottrell, G.A., Clarke, W.H.M. and Gull, S.F., In: *Diagnostics for Fusion Reactor Conditions*, 177. EUR 8351–II EN (1982).

[13] Cottrell, G.A. *Rev. Sci. Instrum.*, **55(9)**, 1401–1409. (1984).

[14] Radon, J., Ber. Ges. Wiss. Leipzig, **69**, 292 (1917).

[15] Bracewell, R.N., *Image Reconstruction from Projections*, ed G.T.Herman (Springer, Berlin) Vol 32, 81 (1979).

[16] de Rosier, D.J. and Klug, Nature, **217**, 130 (1968).

[17] Cottrell, G.A., *J. Phys. E.: Sci. Instrum.*, **15**, 432 (1982).

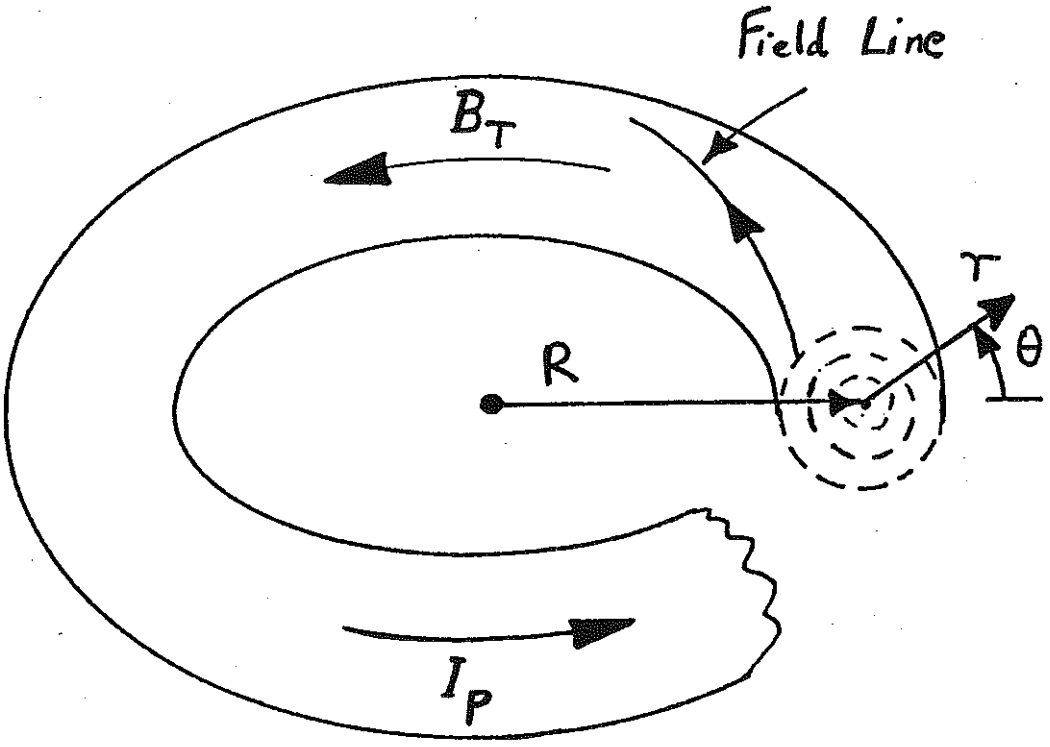

Fig. 1 The main features of a tokamak showing the directions of the toroidal field (B_T) and plasma current (I_p). The major and minor radial coordinates are R and r. Shown by dashed lines are the locations of the magnetic flux surfaces. In the Joint European Torus (JET) tokamak, the major and minor radii are, $R_0 = 2.96$ m, and $a = 1.2$ m with the plasma shape being elongated in the vertical direction by a ratio $b/a < 1.65$.

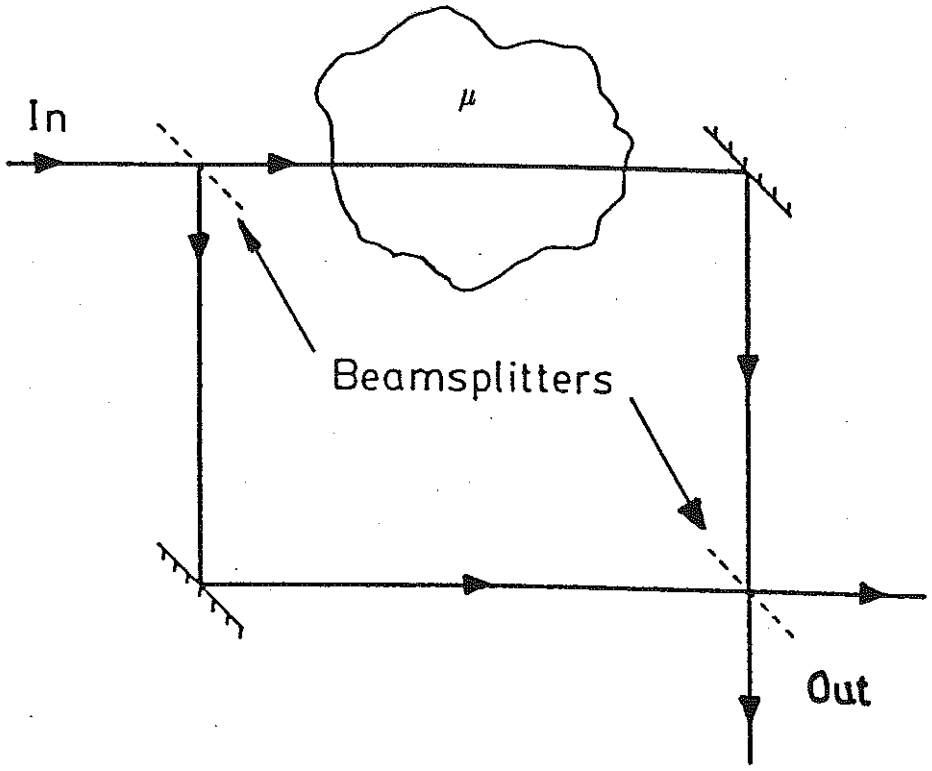

Fig. 2 Mach–Zhender interferometer configuration used to measure the refractive index μ of the plasma.

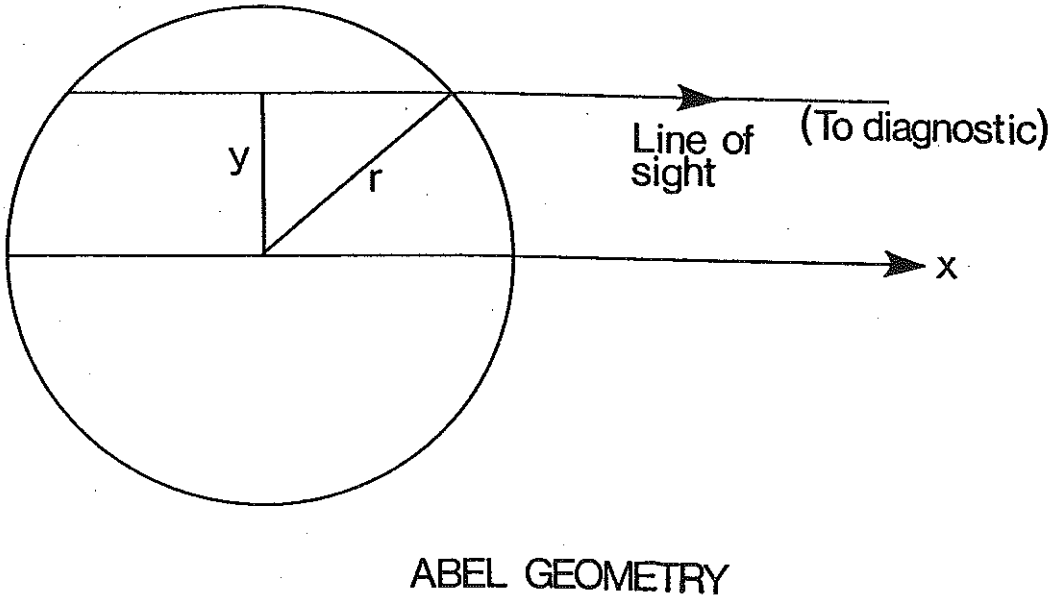

Fig. 3 Geometry assumed for the Abel inversion problem. The diagnostic could be used to measure, for example, the number density of electrons along the line of sight passing through a tokamak plasma.

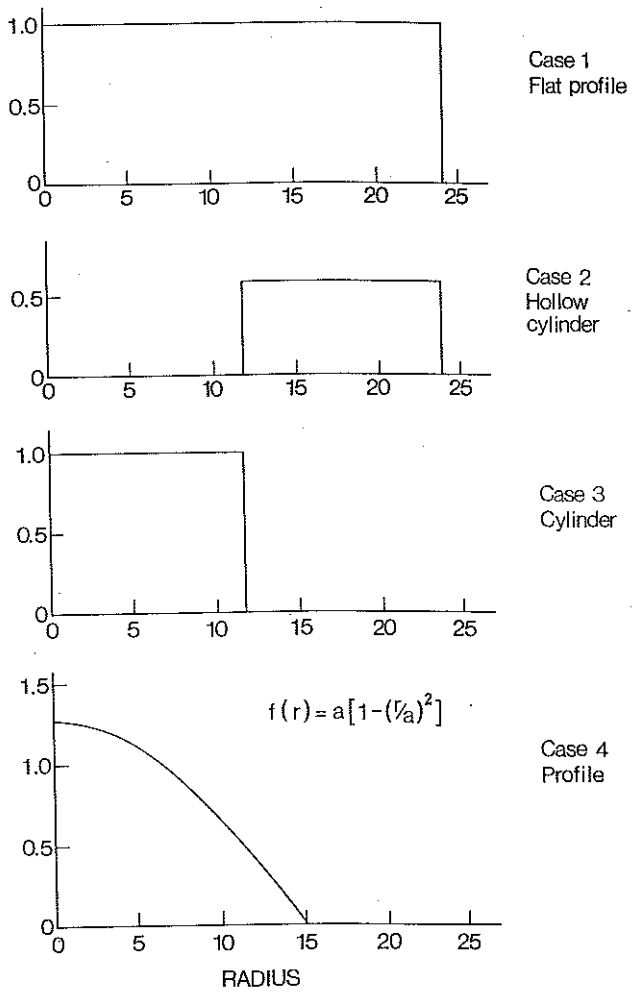

Fig. 4 The four trial functions of electron density versus radius used to generate the simulation line integral data in the Abel inversion problem.

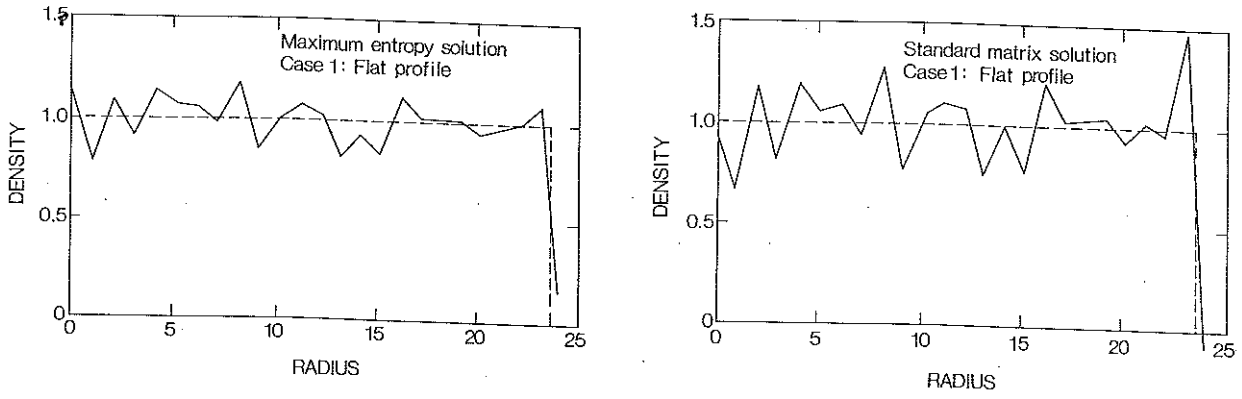

Fig. 5 Reconstructions by MAXENT (upper) and matrix inversion (lower) of the test case 1 (Flat Profile) where the peak signal-to-noise ratio on the simulated line integral data was 20:1.

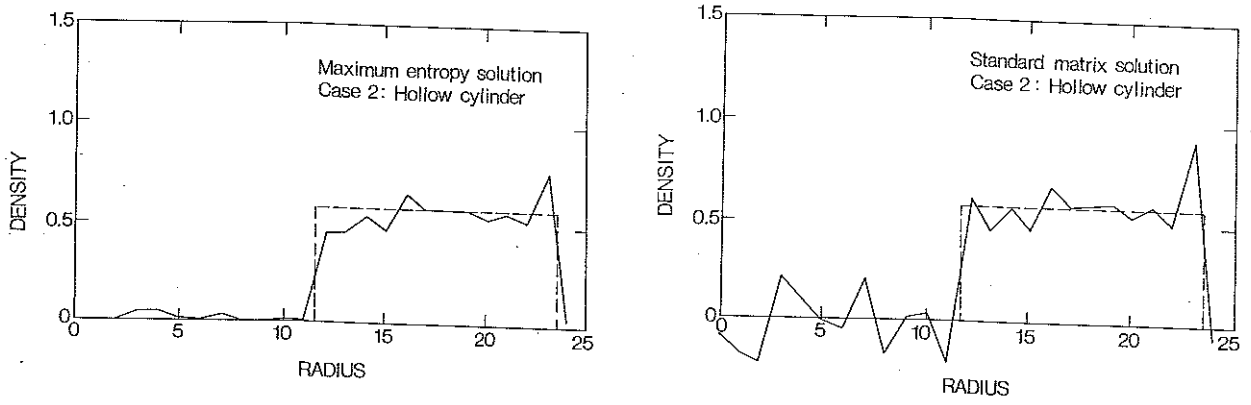

Fig. 6 Reconstructions by MAXENT (upper) and Matrix inversion (lower) of the test case 2 (Hollow Cylinder) where the peak signal-to-noise ratio on the simulated line integral data was 20:1.

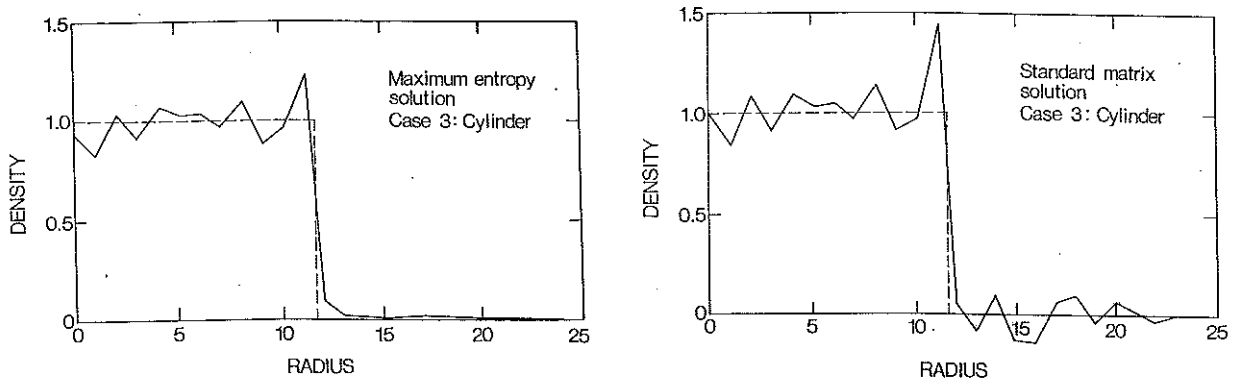

Fig. 7 Reconstructions by MAXENT (upper) and matrix inversion (lower) of the test case 3 (Cylinder) where the peak signal-to-noise ratio on the simulated line integral data was 20:1.

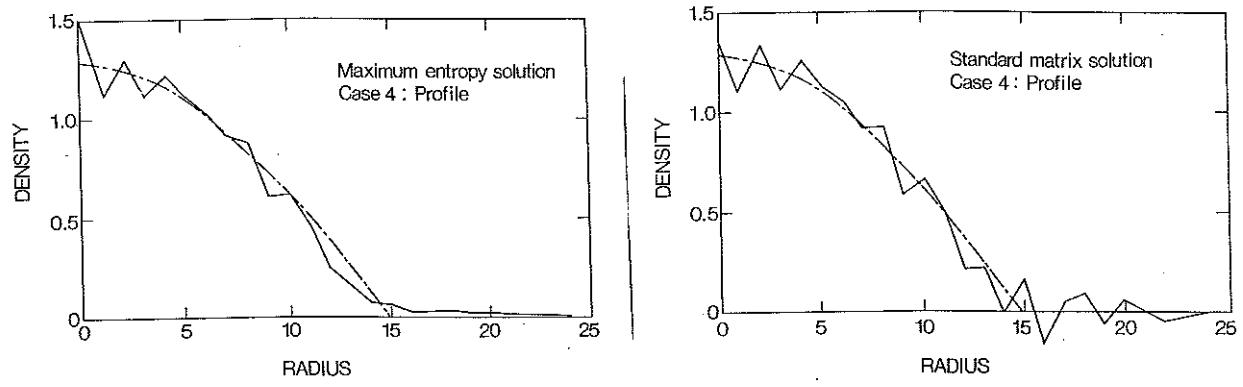

Fig. 8 Reconstructions by MAXENT (upper) and matrix inversion (lower) of the test case 4 (Plasma Profile) where the peak signal-to-noise ratio on the simulated line integral data was 20:1.

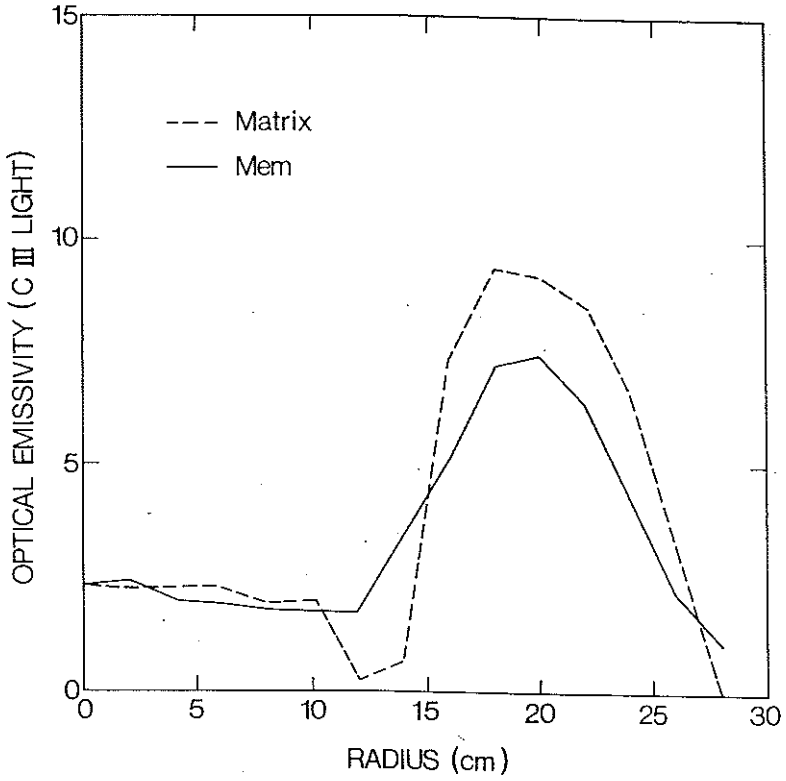

Fig. 9 Abel inverted profiles using both matrix inversion and MAXENT reconstruction of visible CIII radiation emission in DITE tokamak with the bundle divertor switched off (limiter configuration).

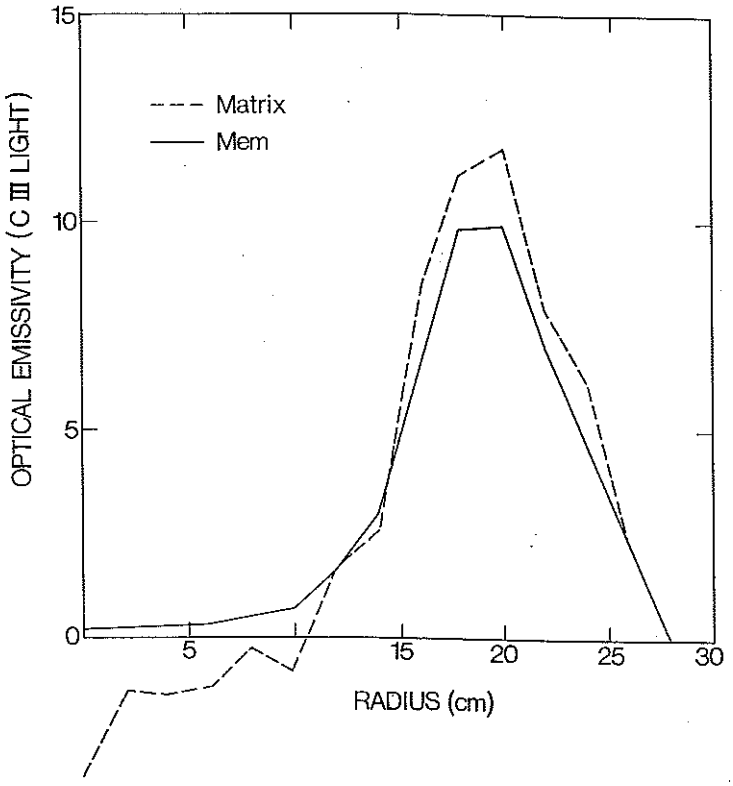

Fig. 10 Abel inverted profiles using both the matrix inversion and MAXENT reconstruction methods of visible CIII radiation emissivity in DITE tokamak with the bundle divertor switched on.

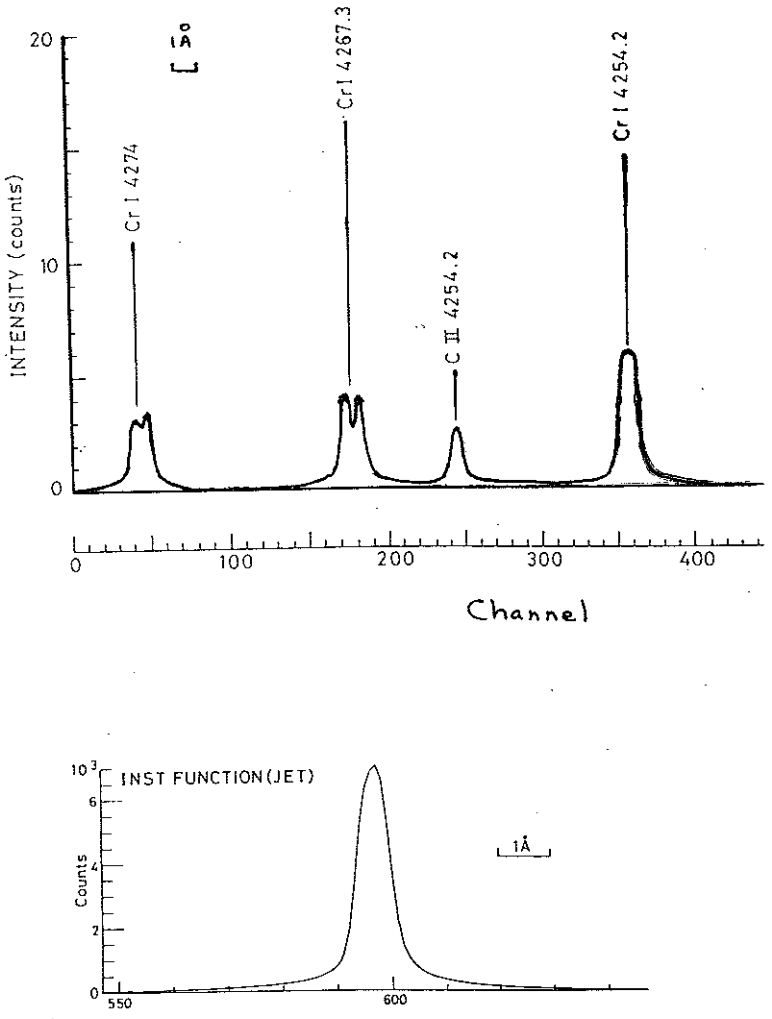

Fig. 11 Visible spectrum from a JET tokamak discharge (raw data) showing some evidence for Zeeman splitting of the Chromium and Carbon spectral emission lines. The spectrometer instrument function is shown below.

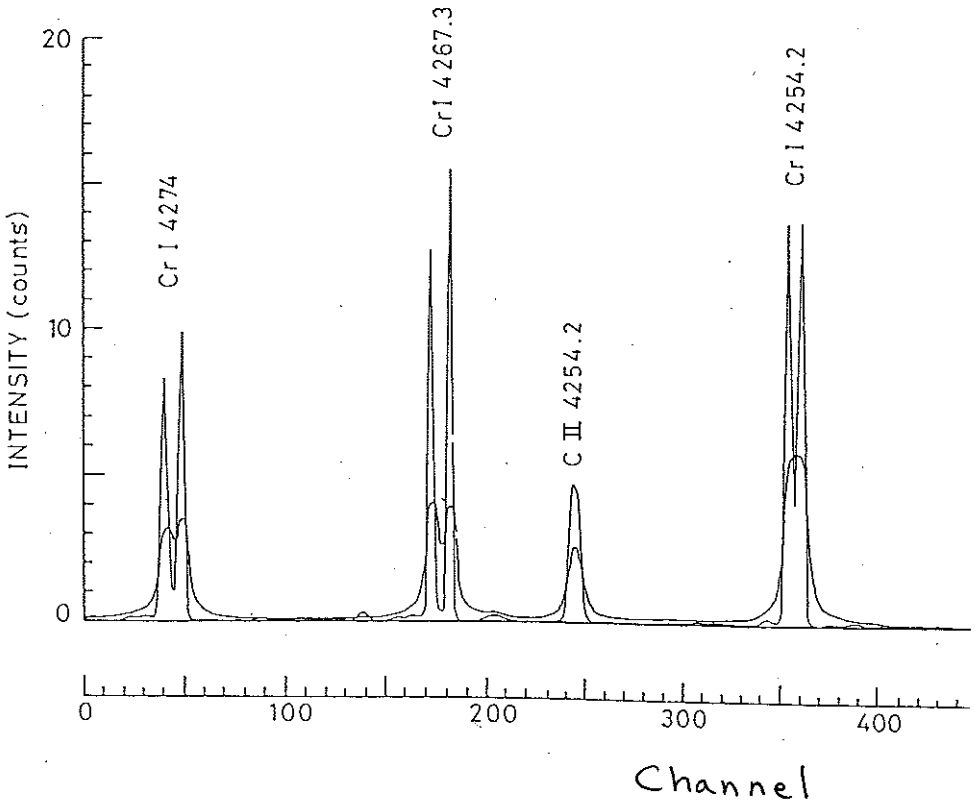

Fig. 12 MAXENT deconvolved spectrum of Fig. 11 superimposed upon the original spectrum.

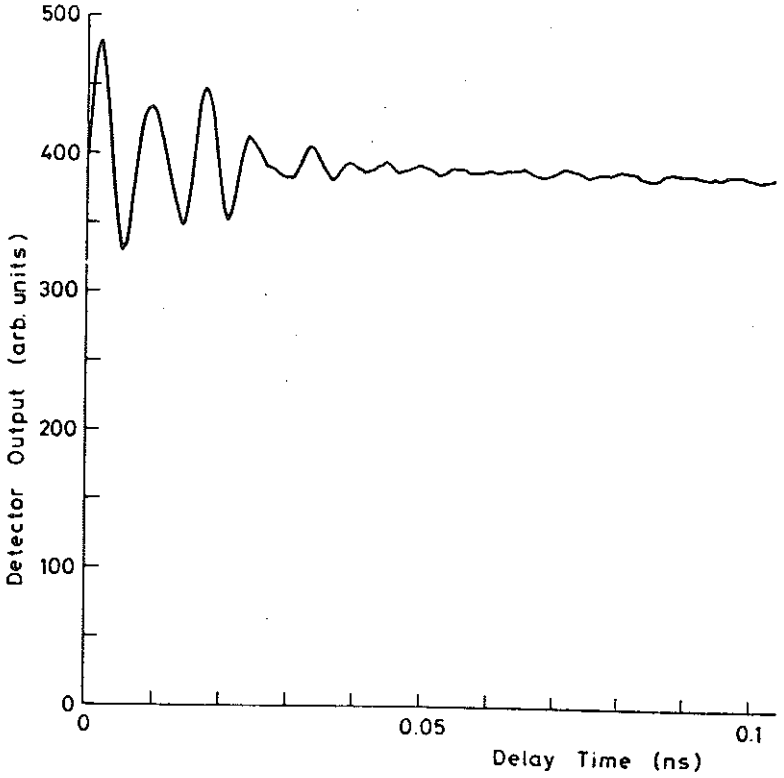

Fig. 13 Experimental autocorrelation data for the Fourier transform spectroscopy technique in which electron cyclotron emission spectra from a tokamak plasma were measured. Here there were N=194 data points in this experiment on a DITE tokamak discharge with a field of 2.2 Tesla. The electron cyclotron frequency was $w_{ce}=61$ GHz.

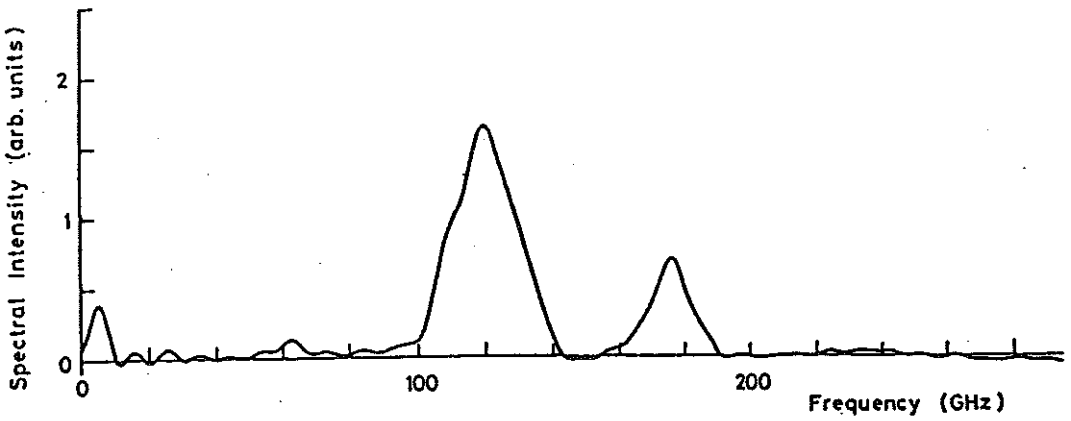

Fig. 14 The Fourier transformed spectrum of the unweighted data in Fig. 13.

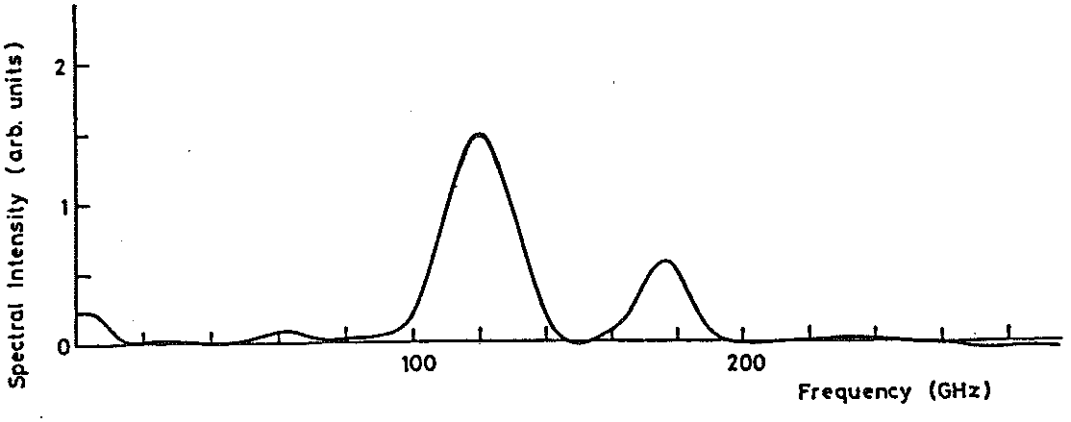

Fig. 15 Cosine squared apodization was applied to the data of Fig. 13 prior to Fourier transformation.

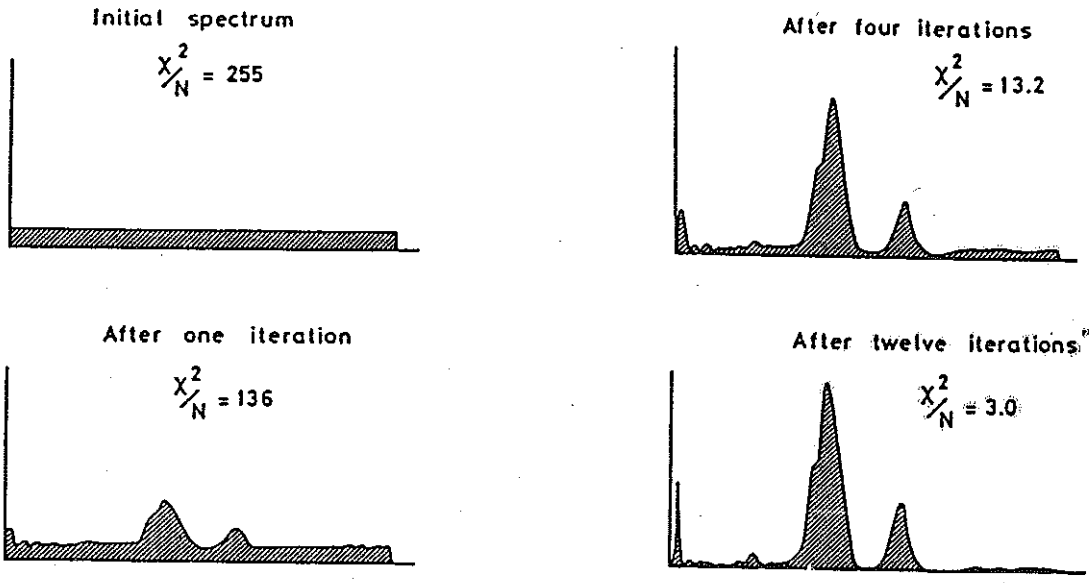

Fig. 16 Development of the reconstructed ECE spectrum during MAXENT iteration on the data of Fig. 13 starting from a flat (initial default level = constant) spectrum. The oversampling rate was $\alpha = 4$, and the zero path difference correction (ZPD) was $\tau_0 = 4.5$ grid points.

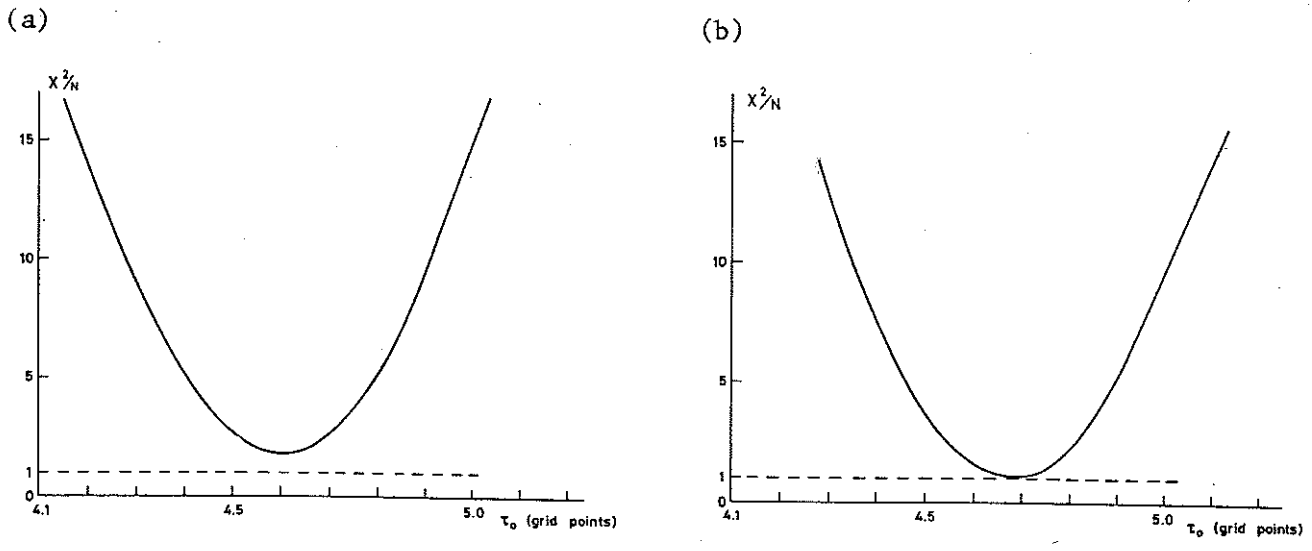

Fig. 17 Example of auto-calibration with MAXENT. In this case the (initially) unknown zero path difference (ZPD) correction was determined iteratively. The process involved minimization of χ^2/N during MAXENT iteration assuming (a) the ZPD correction $\tau_0 = 4.5$ grid points, and (b) the ZPD correction $\tau_0 = 4.68$ grid points.

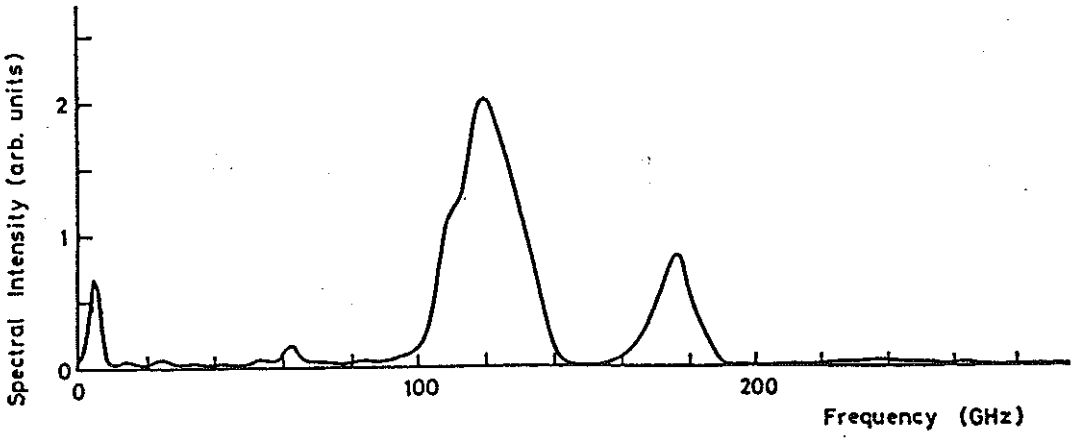

Fig. 18 The final, autocalibrated MAXENT spectrum of electron cyclotron emission.

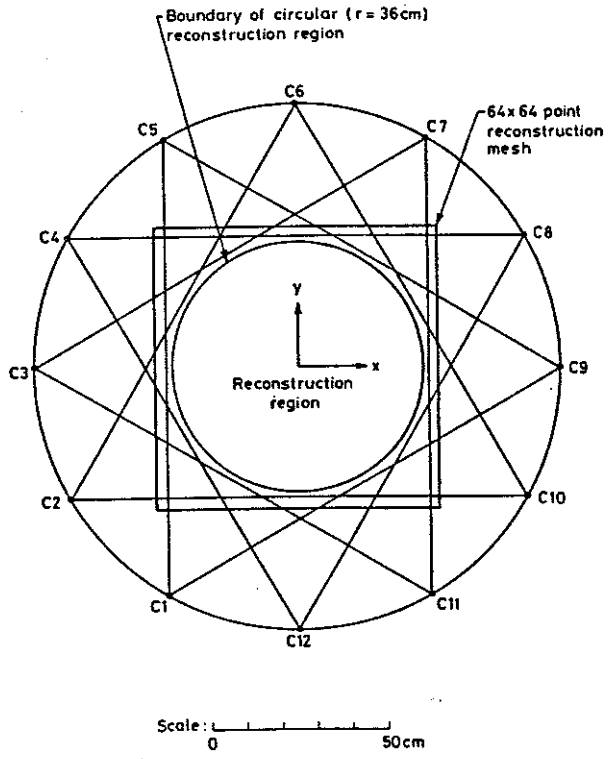

Fig. 19 Geometry of neutral beam scanner system projected onto a cross-section through a test beam-line (the beam propogates in the z-direction). Camera locations are designated $C_1 - C_{12}$ and the lines of sight from each camera are within the viewing limits shown. The inner circle is the reconstruction region lying within the computation mesh. Each camera has an angular resolution of $\approx 1^0$ giving ≈ 60 independent lines of sight per camera. Thus there were up to ≈ 720 lines of sight available to determine the profile of the neutral beam.

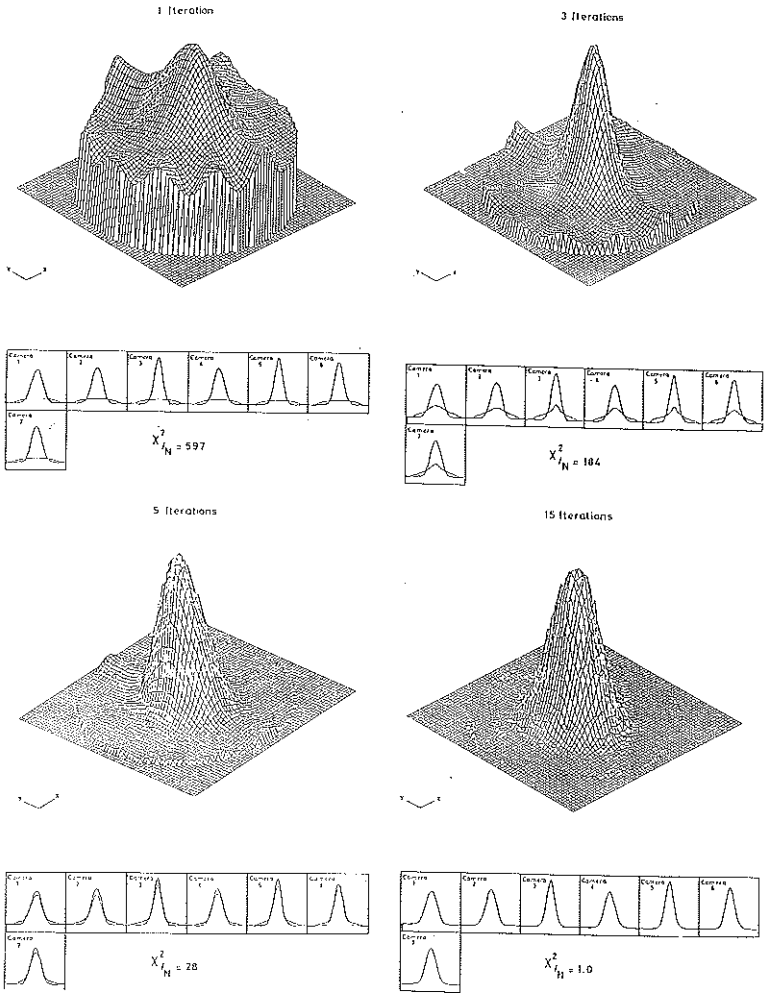

Fig. 20 Development of the MAXENT reconstruction during iteration. Below each isometric projection, the individual camera data are shown (upper curve) as well as the 'mock' data at each iteration (lower curve). After 15 iterations, the two sets of curves merge showing that the data has been fitted by the algorithm, a condition defined by the normalised value of chi–squared reached unity.

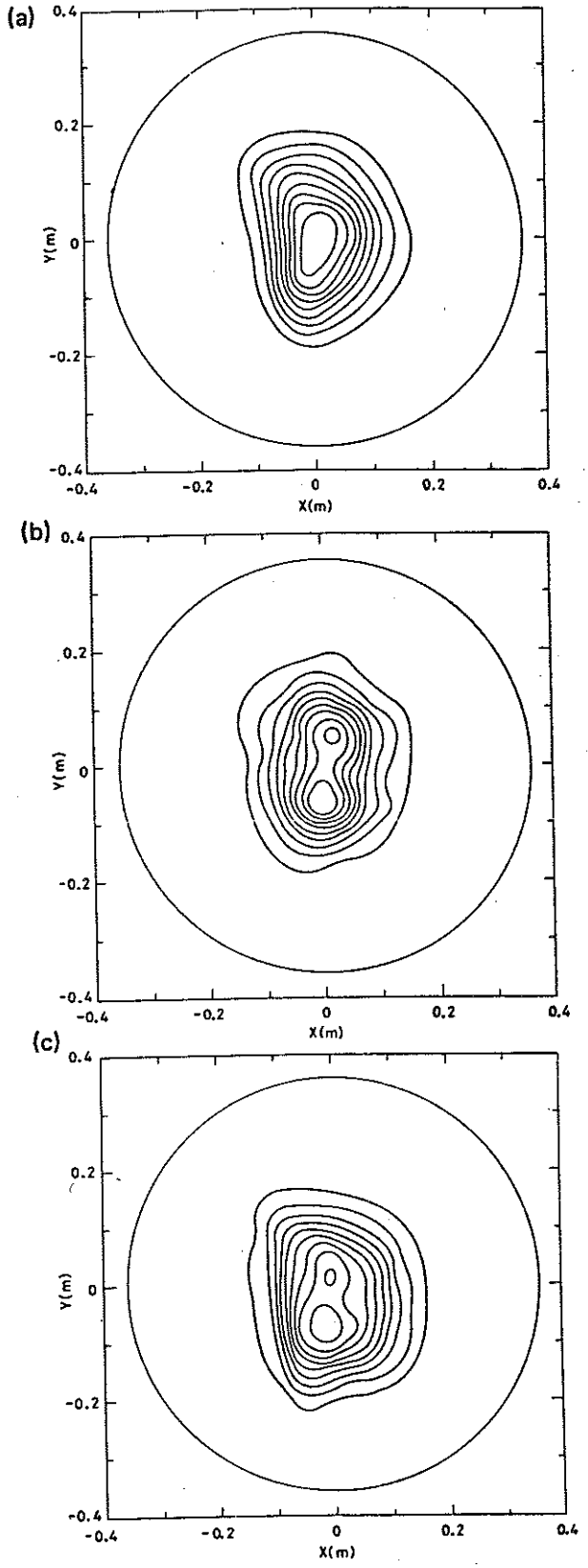

Fig. 21 Tomographic reconstructions showing contours of H_α intensity for beam components with energies (a) E_B, (b) $E_B/2$ and (c) $E_B/3$ corresponding to the extraction and collisional break-up of the molecular ions H^+, H_2^+ and H_3^+ from the ion source. The contour levels were normalized to the peak intensity and are at 10%, 20%, . . . , 90% of the peak level.

APPENDIX 1.

THE JET TEAM

JET Joint Undertaking, Abingdon, Oxon, OX14 3EA, U.K.

J.M.Adams[1], F.Alladio[4], H.Altmann, R.J.Anderson, G.Appruzzese, W.Bailey, B.Balet, D.V.Bartlett, L.R.Baylor[24], K.Behringer, A.C.Bell, P.Bertoldi, E.Bertolini, V.Bhatnagar, R.J.Bickerton, A.Boileau[3], T.Bonicelli, S.J.Booth, G.Bosia, M.Botman, D.Boyd[31], H.Brelen, H.Brinkschulte, M.Brusati, T.Budd, M.Bures, T.Businaro[4], H.Buttgereit, D.Cacaut, C.Caldwell-Nichols, D.J.Campbell, P.Card, J.Carwardine, G.Celentano, P.Chabert[27], C.D.Challis, A.Cheetham, J.Christiansen, C.Christodoulopoulos, P.Chuilon, R.Claesen, S.Clement[30], J.P.Coad, P.Colestock[6], S.Conroy[13], M.Cooke, S.Cooper, J.G.Cordey, W.Core, S.Corti, A.E.Costley, G.Cottrell, M.Cox[7], P.Cripwell[13], F.Crisanti[4], D.Cross, H.de Blank[16], J.de Haas[16], L.de Kock, E.Deksnis, G.B.Denne, G.Deschamps, G.Devillars, K.J.Dietz, J.Dobbing, S.E.Dorling, P.G.Doyle, D.F.Düchs, H.Duquenoy, A.Edwards, J.Ehrenberg[14], T.Elevant[12], W.Engelhardt, S.K.Erents[7], L.G.Eriksonn[5], M.Evrard[2], H.Falter, D.Flory, M.Forrest[7], C.Froger, K.Fullard, M.Gadeberg[11], A.Galetsas, R.Galvao[8], A.Gibson, R.D.Gill, A.Gondhalekar, C.Gordon, G.Gorini, C.Gormezano, N.A.Gottardi, C.Gowers, B.J.Green, F.S.Griph, M.Gryzinski[26], R.Haange, G.Hammett[6], W.Han[9], C.J.Hancock, P.J.Harbour, N.C.Hawkes[7], P.Haynes[7], T.Hellsten, J.L.Hemmerich, R.Hemsworth, R.F.Herzog, K.Hirsch[14], J.Hoekzema, W.A.Houlberg[24], J.How, M.Huart, A.Hubbard, T.P.Hughes[32], M.Hugon, M.Huguet, J.Jacquinot, O.N.Jarvis, T.C.Jernigan[24], E.Joffrin, E.M.Jones, L.P.D.F.Jones, T.T.C.Jones, J.Källne, A.Kaye, B.E.Keen, M.Keilhacker, G.J.Kelly, A.Khare[15], S.Knowlton, A.Konstantellos, M.Kovanen[21], P.Kupschus, P.Lallia, J.R.Last, L.Lauro-Taroni, M.Laux[33], K.Lawson[7], E.Lazzaro, M.Lennholm, X.Litaudon, P.Lomas, M.Lorentz-Gottardi[2], C.Lowry, G.Magyar, D.Maisonnier, M.Malacarne, V.Marchese, P.Massmann, L.McCarthy[28], G.McCracken[7], P.Mendonca, P.Meriguet, P.Micozzi[4], S.F.Mills, P.Millward, S.L.Milora[24], A.Moissonnier, P.L.Mondino, D.Moreau[17], P.Morgan, H.Morsi[14], G.Murphy, M.F.Nave, M.Newman, L.Nickesson, P.Nielsen, P.Noll, W.Obert, D.O'Brien, J.O'Rourke, M.G.Pacco-Düchs, M.Pain, S.Papastergiou, D.Pasini[20], M.Paume[27], N.Peacock[7], D.Pearson[13], F.Pegoraro, M.Pick, S.Pitcher[7], J.Plancoulaine, J-P.Poffé, F.Porcelli, R.Prentice, T.Raimondi, J.Ramette[17], J.M.Rax[27], C.Raymond, P-H.Rebut, J.Removille, F.Rimini, D.Robinson[7], A.Rolfe, R.T.Ross, L.Rossi, G.Rupprecht[14], R.Rushton, P.Rutter, H.C.Sack, G.Sadler, N.Salmon[13], H.Salzmann[14], A.Santagiustina, D.Schissel[25], P.H.Schild, M.Schmid, G.Schmidt[6], R.L.Shaw, A.Sibley, R.Simonini, J.Sips[16], P.Smeulders, J.Snipes, S.Sommers, L.Sonnerup, K.Sonnenberg, M.Stamp, P.Stangeby[19], D.Start, C.A.Steed, D.Stork, P.E.Stott, T.E.Stringer, D.Stubberfield, T.Sugie[18], D.Summers, H.Summers[20], J.Taboda-Duarte[22], J.Tagle[30], H.Tamnen, A.Tanga, A.Taroni, C.Tebaldi[23], A.Tesini, P.R.Thomas, E.Thompson, K.Thomsen[11], P.Trevalion, M.Tschudin, B.Tubbing, K.Uchino[29], E.Usselmann, H.van der Beken, M.von Hellermann, T.Wade, C.Walker, B.A.Wallander, M.Walravens, K.Walter, D.Ward, M.L.Watkins, J.Wesson, D.H.Wheeler, J.Wilks, U.Willen[12], D.Wilson, T.Winkel, C.Woodward, M.Wykes, I.D.Young, L.Zannelli, M.Zarnstorff[6], D.Zasche[14], J.W.Zwart.

PERMANENT ADDRESS

1. UKAEA, Harwell, Oxon. UK.
2. EUR-EB Association, LPP-ERM/KMS, B-1040 Brussels, Belgium.
3. Institute National des Récherches Scientifique, Quebec, Canada.
4. ENEA-CENTRO Di Frascati, I-00044 Frascati, Roma, Italy.
5. Chalmers University of Technology, Göteborg, Sweden.
6. Princeton Plasma Physics Laboratory, New Jersey, USA.
7. UKAEA Culham Laboratory, Abingdon, Oxon. UK.
8. Plasma Physics Laboratory, Space Research Institute, Sao José dos Campos, Brazil.
9. Institute of Mathematics, University of Oxford, UK.
10. CRPP/EPFL, 21 Avenue des Bains, CH-1007 Lausanne, Switzerland.
11. Risø National Laboratory, DK-4000 Roskilde, Denmark.
12. Swedish Energy Research Commission, S-10072 Stockholm, Sweden.
13. Imperial College of Science and Technology, University of London, UK.
14. Max Planck Institut für Plasmaphysik, D-8046 Garching bei München, FRG.
15. Institute for Plasma Research, Gandhinagar Bhat Gujat, India.
16. FOM Instituut voor Plasmafysica, 3430 Be Nieuwegein, The Netherlands.
17. Commissiariat à L'Energie Atomique, F-92260 Fontenay-aux-Roses, France.
18. JAERI, Tokai Research Establishment, Tokai-Mura, Naka-Gun, Japan.
19. Institute for Aerospace Studies, University of Toronto, Downsview, Ontario, Canada.
20. University of Strathclyde, Glasgow, G4 ONG, U.K.
21. Nuclear Engineering Laboratory, Lapeenranta University, Finland.
22. JNICT, Lisboa, Portugal.
23. Department of Mathematics, Univeristy of Bologna, Italy.
24. Oak Ridge National Laboratory, Oak Ridge, Tenn., USA.
25. G.A. Technologies, San Diego, California, USA.
26. Institute for Nuclear Studies, Swierk, Poland.
27. Commissiariat à l'Energie Atomique, Cadarache, France.
28. School of Physical Sciences, Flinders University of South Australia, South Australia SO42.
29. Kyushi University, Kasagu Fukuoka, Japan.
30. Centro de Investigaciones Energeticas Medioambientales y Techalogicas, Spain.
31. University of Maryland, College Park, Maryland, USA.
32. University of Essex, Colchester, UK.
33. Akademie de Wissenschaften, Berlin, DDR.

CR 88.49.1A